Reconfigurable spin-wave platform based on interplay between nanodots and waveguide in hybrid magnonic crystal

Krzysztof Szulc,* Mateusz Zelent, and Maciej Krawczyk
Institute of Spintronics and Quantum Information,
Faculty of Physics, Adam Mickiewicz University, Poznań,
Uniwersytetu Poznańskiego 2, 61-614 Poznań, Poland
(Dated: April 17, 2024)

We present a hybrid magnonic crystal composed of a chain of nanodots with strong perpendicular magnetic anisotropy and Dzyaloshinskii–Moriya interaction, positioned above a permalloy waveguide. The study examines two different magnetization states in the nanodots: a single-domain state and an egg-shaped skyrmion state. Due to the dipolar coupling between the dot and the waveguide, a strongly bound hybrid magnetization texture is formed in the system. Our numerical results show complex spin-wave spectra, combining the effects of periodicity, magnetization texture, and hybridization of the propagating waves in the waveguide with the dot/skyrmion modes. The systems are characterized by different band gap sizes. For the skyrmion state, the azimuthal modes confined to the skyrmion domain wall lead to the formation of flat bands at low frequencies, while at higher frequencies we identify among them modes interacting with the propagating waves, which can introduce additional non-Bragg band gaps, as well as isolated modes leading to the formation of bound states. On the other hand, the system with a single-domain state in nanodots offers a wide range of frequencies where the spin waves are predominantly in the waveguide. Thus, the study shows that the proposed hybrid magnonic crystals have many distinct functionalities, highlighting their reconfigurable potential, magnon–magnon couplings, mode localization, and bound states overlapping with the propagating waves. This opens up potential applications in analog and quantum magnonics, spin-wave filtering, and the establishment of magnonic neural networks.

I. INTRODUCTION

Over the past decade, spin-wave (SW) computing has been extensively researched as a potential candidate to complement and surpass CMOS-based technologies [1, 2] for digital [3] or analog signal processing [4, 5] and neural network implementation [6, 7]. This is because SWs offer high-frequency operation, even at tens of GHz, miniaturization down to the nanoscale, well below 100 nm, and most importantly, ultralow power consumption, as low as 1 aJ per operation. Moreover, they can locally interact with magnetic solitons, i.e. domain walls in 1D and magnetic vortices or skyrmions in 2D, and thus can hybridize with, be excited by, and be controlled by soliton dynamics [8–10].

Magnetic skyrmions are topologically protected 2D magnetization textures, known for their stability and very small size, especially Néel skyrmions in thin ferromagnetic films, which are stabilized by Dzyaloshinskii–Moriya interaction (DMI) [11]. Their dynamics can be driven by external forces such as magnetic field, electric current, structural stress, thermal fluctuations, or laser pulses [12], which expands their possible applications also in magnonics, e.g., to control wave propagation [13], scatter SWs [14], form SW frequency combs [15], or to excite propagating SWs [16] in thin films. This makes them promising candidates for information storage and processing [17–20]. In particular, their potential has attracted considerable interest in non-Boolean logic and unconventional computing devices [21–23]. However, due to the high damping of SWs in multilayers possessing DMI [24, 25], with a few exceptions those effects remain mainly numerical demonstrations [26].

In a skyrmion within confined geometry, three types of eigenmodes have been observed [27, 28]: gyroscopic, breathing, and azimuthal modes. The gyroscopic mode refers to the rotational motion of the skyrmion core [29]. The breathing mode involves the radial oscillation of the size of the skyrmion [30]. Azimuthal modes are SWs propagating along the skyrmion circumference [31–33]. Their quantization is described by an azimuthal wave number, with clockwise (CW) and counterclockwise (CCW) degeneracy lifted by the asymmetric exchange interaction. When the dots are arranged in a chain or array, bands of collective skyrmion excitations can be formed [34]. However, the dynamic dipolar coupling between the skyrmions is rather weak, especially between the azimuthal modes, and the non-zero bandwidths have been numerically demonstrated only for gyrotropic or breathing modes [31].

Hybrid structures are commonly used to obtain systems that combines two, usually mutually exclusive, material properties, such as ferromagnetism and superconductivity [35]. This is also true for magnonics and skyrmions. The former requires long propagation distances and thus low damping, while the latter requires DMI resulting from spin–orbit interactions and heavy neighboring metals, which is associated with increased damping. The bilayer structure composed of yttrium iron garnet and the Co/Pt multilayer with the skyrmion has been proposed as a point source to excite short SWs with

* krzysztof.szulc@amu.edu.pl

tens of nm wavelength [36].

We propose a hybrid structure consisting of a SW conduit made of a low-damping material (Py) and a chain of (Ir/Co/Pt) nanodots of 300 nm diameter, forming a hybrid magnonic crystal (HMC) that serves as a multifunctional platform for SW applications. Such an HMC structure has shown an extended range of DMI values, which facilitates Néel-type skyrmion stabilization at comparatively lower DMI values [37]. Using micromagnetic simulations, we show that this HMC exhibits several interesting properties arising from the coupling between the subsystems relevant to control SWs. These include flat magnonic bands both below and above the bottom of the SW spectrum in Py, and a reprogrammable magnonic band structure, where the width of the band gaps is modified by the magnetization texture in the dots at the remanence: skyrmion or single-domain state. The former property provides a system for the realization of bound states in the continuum in a magnonic domain [38], the latter for the SW filtering or Bose–Einstein condensation realization [39]. Moreover, the dynamic coupling between SWs propagating in the waveguide and SWs confined to the domain wall of the skyrmion results in band anticrossing, making this system suitable for exploiting the magnon–magnon coupling, and thus useful for quantum magnonics applications [40]. Taking into account the multifunctionality, the proposed HMCs represent a promising platform for magnonic artificial neural networks, as proposed in Ref. [41], or where the waveguide serves as synapses connected by propagating SWs, and interacting resonant neurons, i.e. nanodots on the waveguide with the rich spectra of SW modes [42]. The complex interactions between propagating SWs and nanodisks discussed in this paper open avenues for creating tunable artificial neurons.

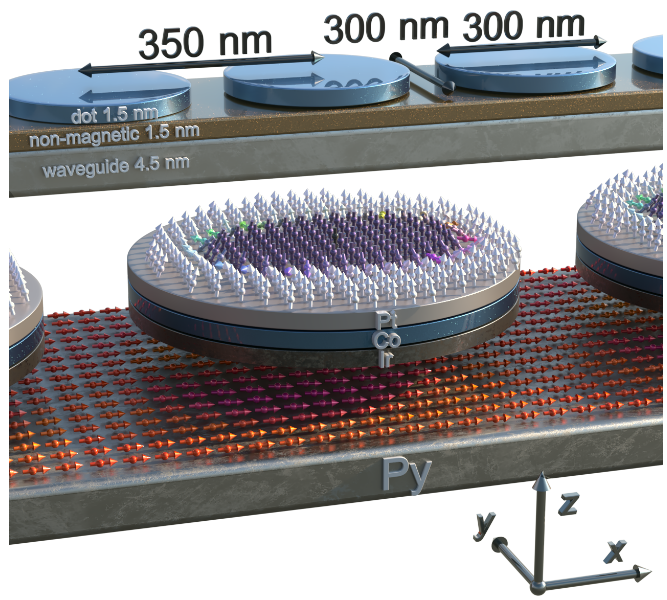

Figure 1. The visual representation of the system under consideration. The Ir/Co/Pt multilayer dot is separated from the 4.5 nm-thick Py strip by a 3 nm-thick nonmagnetic layer. In the dot, an egg-shaped Néel-type skyrmion is stabilized by the magnetostatic coupling to the skyrmion imprint on the in-plane magnetized strip. The arrows and their color (according to the HSL-cone color scale) indicate the direction of magnetization. Note that the figure is not to scale.

II. METHODS

The system under investigation is presented in Fig. 1. It consists of the infinitely-long waveguide made of permalloy (Py, $Ni_{80}Fe_{20}$) with a width of 300 nm and a thickness of 4.5 nm and a chain of Co dots with a 300 nm diameter and 1.5 nm thickness. The dots are laying centrally above the waveguide with a relative separation of 50 nm, resulting in the periodic structure with a lattice constant of 350 nm. The waveguide and the dots are separated by a 3 nm-thick nonmagnetic layer.

The magnetization dynamics of the system are described by the Landau–Lifshitz–Gilbert equation:

$$\frac{\partial \mathbf{M}}{\partial t} = -|\gamma|\mu_0 \mathbf{M} \times \mathbf{H}_{\mathrm{eff}} + \frac{\alpha}{M_{\mathrm{S}}} \mathbf{M} \times \frac{\partial \mathbf{M}}{\partial t}, \quad (1)$$

where γ is the gyromagnetic ratio, μ_0 is the magnetic permeability of vacuum, $\mathbf{H}_{\mathrm{eff}}$ is the effective magnetic field, α is the damping constant, and M_{S} is the saturation magnetization. The effective magnetic field $\mathbf{H}_{\mathrm{eff}}$ is described as follows:

$$\begin{aligned}\mathbf{H}_{\mathrm{eff}} = \mathbf{H}_0 + \frac{2A_{\mathrm{ex}}}{\mu_0 M_{\mathrm{S}}^2}\nabla^2\mathbf{M} + \frac{2K_{\mathrm{PMA}}}{\mu_0 M_{\mathrm{S}}^2} M_z \hat{\mathbf{z}} - \nabla\varphi + \\ + \frac{2D}{\mu_0 M_{\mathrm{S}}^2}\left(\frac{\partial M_z}{\partial x}\hat{\mathbf{x}} + \frac{\partial M_z}{\partial y}\hat{\mathbf{y}} - \left(\frac{\partial M_x}{\partial x} + \frac{\partial M_y}{\partial y}\right)\hat{\mathbf{z}}\right),\end{aligned} \quad (2)$$

where $\mathbf{H}_0$ is the external magnetic field, A_{ex} is the exchange stiffness constant, K_{PMA} is the perpendicular magnetic anisotropy constant, D is the Dzyaloshinskii–Moriya constant, and φ is the magnetic scalar potential, which can be determined from the formula

$$\nabla^2\varphi = \nabla \cdot \mathbf{M}, \quad (3)$$

which is derived from Maxwell equations in the magnetostatic approximation.

The system was studied using the finite-element method simulations in COMSOL Multiphysics [43]. The simulations were performed in the 3D model with the implementation of Eqs. (1) and (3). The static magnetization configuration was stabilized in the time-domain simulation with periodic boundary conditions placed at the ends of the unit cell perpendicular to the x-axis to introduce the periodicity into the system. For the proper calculation of the stray magnetic field, the condition $\varphi = 0$ is applied at a distance of 10 µm from the system. As an initial magnetization configuration, the waveguide is uniformly magnetized along the x-axis while the dots are uniformly magnetized along the z-axis (for the study of a single-domain state configuration) or have a skyrmion inside (for the study of skyrmion state) [44]. The magnetic state relaxation lasts 1 µs. The dispersion relation was calculated using the eigenfrequency solver. For this purpose, the Landau–Lifshitz–Gilbert equation is solved in its linearized form, where the total magnetization vector $\mathbf{M} = \mathbf{M}_0 + \mathbf{m}\, e^{i\omega t}$ is splitted to a static component $\mathbf{M}_0 = (M_{0x}, M_{0y}, M_{0z})$ and a dynamic component $\mathbf{m} = (m_x, m_y, m_z)$. The equation takes the form of an eigenvalue equation, where the complex eigenvalues give the frequencies, the dynamic magnetization $\mathbf{m}$ and the dynamic magnetic scalar potential are the eigenvectors, and the wavevector is a sweep parameter. Here, the periodic boundary conditions are replaced by Bloch boundary conditions. The tetrahedral mesh is used with a maximum size of 5 nm in the dot and 7 nm in the waveguide. Outside the magnetic material, the mesh grows with ratio 1.4. On the sides where Bloch boundary condition is applied, we prepared identical triangular meshes.

The material parameters of Py are $M_\mathrm{S} = 800\,\mathrm{kA/m}$, $A_\mathrm{ex} = 13\,\mathrm{pJ/m}$, $D = 0$, $K_\mathrm{PMA} = 0$, $\alpha = 0.005$. The magnetic dot is defined with an effective-medium approach [45–48] as a structure with DMI and PMA, where the three repetitions of the 0.5 nm-thick Ir/Co/Pt multilayer are simulated as a single Co layer with an effective thickness. The effective parameters of the dot are $M_\mathrm{S} = 956\,\mathrm{kA/m}$, $A_\mathrm{ex} = 10\,\mathrm{pJ/m}$, $D = -1.6\,\mathrm{mJ/m^2}$, $K_\mathrm{PMA} = 717\,\mathrm{kJ/m^3}$, $\alpha = 0.02$. In all calculations, the external magnetic field $\mathbf{H}_0 = 0$.

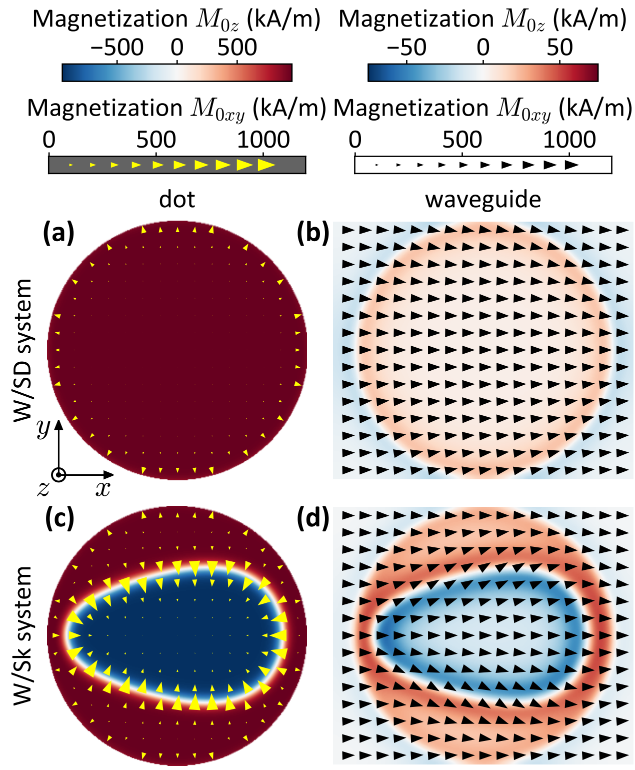

Figure 2. Configuration of the magnetization in the unit cell of the coupled system of waveguide with the chain of dots in (a,b) the single-domain state and (c,d) skyrmion state. The magnetization is shown in the xy-planes crossing (a,c) the center of the dot and (b,d) the center of the waveguide. The color map shows the M_{0z} component of the magnetization, and the in-plane component M_{0xy} is presented with the arrows.

III. RESULTS AND DISCUSSION

A. Static magnetization texture

First, let us consider the waveguide and nanodot subsystems separately, focusing on the static magnetic configuration of the system in the absence of an external magnetic field. In the multilayer nanodot, characterized by strong PMA and DMI, various magnetization states can be stabilized, including an out-of-plane single-domain state, a Néel-type skyrmion, a double-domain structure, and a worm-like domains [49]. In this paper, we are focusing on two of the above-mentioned configurations—a single-domain state (SD) and a skyrmion state (Sk). While the literature is well-versed in the static and dynamic behavior of these structures in isolation [33, 50], their static and dynamic properties become complex in a compact hybrid system [37].

Figure 2 presents the static magnetic configuration of a single unit cell of the HMC. Here, we consider hybrid systems with two different magnetization configurations—the waveguide (W) with a chain of dots with the single-domain out-of-plane magnetization state (W/SD) and the waveguide with a chain of dots with skyrmions (W/Sk). The magnetization texture is shown on the xy-planes crossing the center of the dot (a,c) and the center of the waveguide (b,d), respectively. In the HMC, the magnetization configuration differs from that of isolated subsystems. This change, induced by the dipolar coupling, is mainly caused by the competition between the strong PMA in the dots, which favors magnetization along the z-axis, and the shape anisotropy inherent in the waveguide, which induces a preference for magnetization along the x-axis.

In the W/SD system, the most pronounced effect of dipolar interaction between the subsystems manifests just beneath the edges of the dot, as illustrated in Fig. 2(b). Here, the peak deviation in magnetization reaches $\max|M_{0y}| = 216$ kA/m along the y-axis and $\max|M_{0z}| = 23$ kA/m along the z-axis. Notably, within the nanodot itself, the magnetization deviation of approximately 2% is present close to the dot edge.

The static magnetic texture in the W/Sk system undergoes more significant modification. Unlike the configurations observed in the individual subsystems, the skyrmion is not only imprinted in the waveguide, but also takes on an egg-like shape instead of being circular. This static effect has already been demonstrated in the system with a single dot and finite strip in Ref. [37]. Please note that the imprint intensity is stronger in the W/Sk system than in the W/SD system. The average net magnetization along the easy axis in the W/Sk system decreases by 20 kA/m in comparison with only 5 kA/m for W/SD system. Also, the maximum deviation reaches $\max|M_{0y}| = 475$ kA/m and $\max|M_{0z}| = 59$ kA/m.

B. Spin-wave dynamics

Following the analysis of the static magnetization configurations of the system, we performed numerical simulations of the SW dynamics. The dispersion relations of W/SD and W/Sk systems are depicted in Fig. 3(a) and Fig. 3(b), respectively, where the color map indicates the intensity I of the out-of-plane dynamic magnetization component m_z across the entire system. The intensity of each mode is quantified as follows:

$$I_{\mathrm{mode}}(k, f_n(k)) = \left| \iiint_V m_z(f_n(k)) e^{ikx} \,\mathrm{d}x\,\mathrm{d}y\,\mathrm{d}z \right|^2, \quad (4)$$

where V denotes the volume of magnetic material within a single unit cell and $f_n(k)$ is the frequency of the nth mode at wavevector k. Next, the intensities of all modes are converted into the Lorentzian function and then summed to give the total intensity I

$$I(k, f) = \sum_n \frac{I_{\mathrm{mode}}(k, f_n(k))}{\mathrm{Im}[f_n(k)] \left(1 + \left(\frac{f - \mathrm{Re}[f_n(k)]}{\mathrm{Im}[f_n(k)])}\right)^2\right)} \quad (5)$$

at wavevector k and frequency f. This method of quantifying intensity makes these results comparable to the Brillouin light scattering measurement results [51]. For comparison, the dispersion relation of an isolated waveguide without a chain of dots is illustrated with dashed black lines. The comparison between the dispersion relation of the isolated waveguide and the frequencies of the SW modes in the isolated dot in the single-domain and skyrmion states is presented in Section S1 of the Supplementary Materials.

The dispersion relations of both systems contain complex mode dependencies, caused by the interaction between the dots and their imprints in the waveguide. The highest-intensity mode follows the fundamental mode of an isolated waveguide. The antisymmetric waveguide modes are barely visible in the plots due to the nature of the intensity calculation. Above the third waveguide mode, the intensity distribution is unclear and only the fundamental modes are recognizable. The reflected branches and band gaps are present as a result of the periodicity induced by the arrangement of the dots.

However, there are significant differences in the band-gap width of the Bragg gaps among the systems. The zoom-ins of the dispersions of W/SD and W/Sk systems are shown in Fig. 3(c) and Fig. 3(d), respectively, with gray strips marking the positions of the band gaps. The widths of the first five band gaps are listed in Fig. 3(e). The W/SD system is characterized by larger low-order gaps, with the size exceeding 400 MHz. The size of higher-order gaps is much smaller, with gap 5 already being similar in size to the linewidth of the modes (which is 77 MHz), making it barely noticeable. In contrast, the W/Sk system is characterized by larger sizes of higher-order band gaps, i.e., third and higher. Interestingly, the first band gap is completely absent. Due to the backward wave character of the mode at low wavevectors, the edge of the first Brillouin zone lies close to the frequency minimum. As a result, the first and second bands share the same character. In the W/SD system, the stronger interaction between the modes pushes the first band much below the frequency of the isolated waveguide (see Fig. 3(a)). In the W/Sk system, this interaction is weaker, which causes the first band maximum to be at a higher frequency than the second band minimum, leading to the absence of the band gap, as visible in Fig. 3(d). These properties clearly demonstrate the reprogrammable nature of the proposed HMC system. By preserving the frequency positions of the band gaps, we can modify their width and even close or open the first band gap simply by changing the magnetization state in the dots.

Another difference is the presence of numerous flat bands in the dispersion of the W/Sk system, which lie below the waveguide modes and begin at frequencies below 1 GHz. These modes are directly connected to the dynamics of the skyrmion domain wall in the dots which starts at the level of hundreds of MHz (see, Fig. S1 in the Supplementary Materials). At higher frequencies, some of the skyrmion modes hybridize with the waveguide modes. Interestingly, one of these modes leads to the generation of an additional band gap with a width of 53 MHz, marked as gap 3a in Fig. 3(d). The modified spectra indicate that the presence of skyrmions in dots can directly affect the dynamics of SWs propagating in the waveguide. Obviously, such modes are not present in the W/SD system since the lowest resonant mode of the dot in a single-domain state is at the frequency of 9 GHz, which is above the third waveguide mode. These results show that the change of a magnetization configuration of the dots can induce additional flat bands in the SW spectrum and also magnon–magnon coupling, effects which are currently under intense investigation and also important from an application point of view. In the next section, we will explore these properties, focusing on understanding of the physical mechanisms involved.

C. Mode localization

In order to deepen the analysis of the SW dynamics in both systems, we calculated the localization of the modes and plotted it on the dispersion relation folded to the first Brillouin zone as shown in Fig. 4(b) and (c). We define

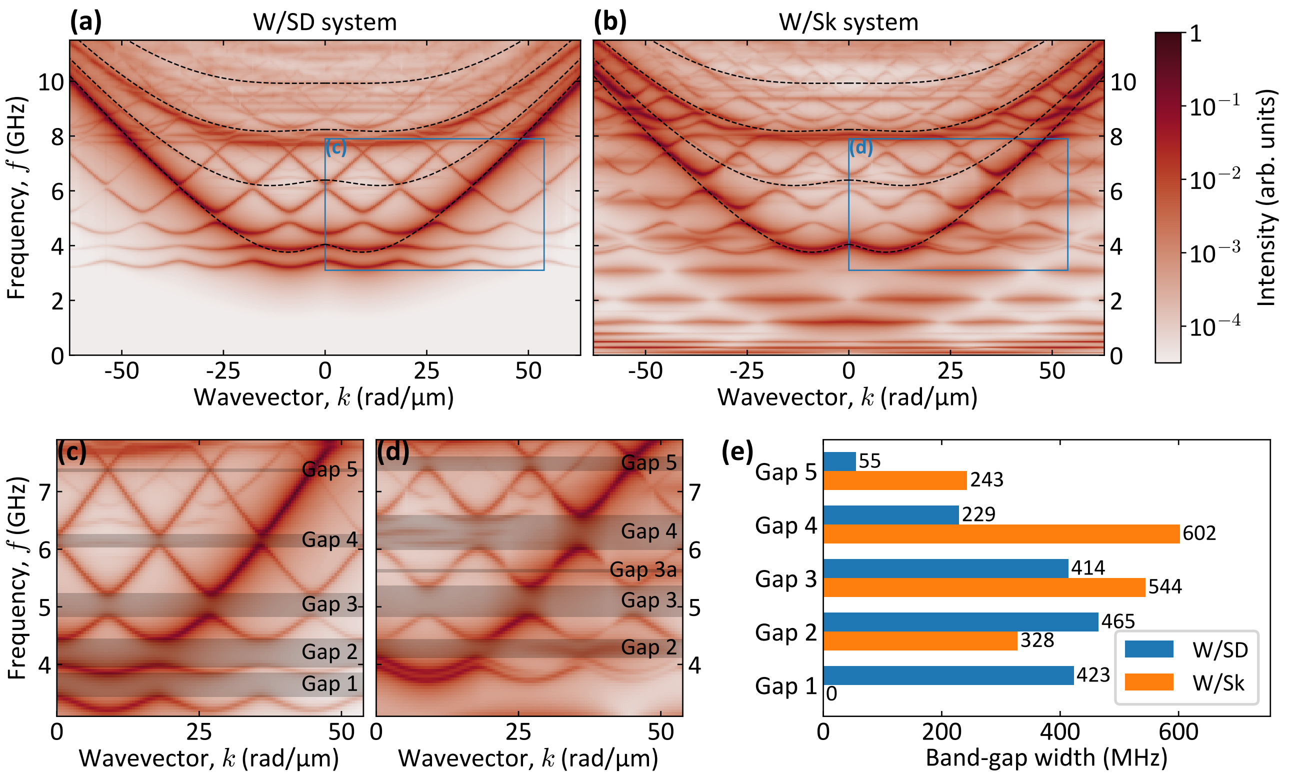

Figure 3. Dispersion relation of (a) the W/SD system and (b) the W/Sk system. Color maps show the intensity measured for the out-of-plane component of the magnetization m_z. Intensity is scaled logarithmically. Dashed black lines show the dispersion relation of waveguide itself without dots. Subfigures (c) and (d) are zoom-ins of the W/SD and W/Sk systems' dispersion relations as marked by blue rectangles in subfigures (a) and (b), respectively. Gray rectangles mark the Bragg gaps in the dispersion relation. (e) Bar chart collecting band-gap widths for both W/SD and W/Sk systems.

the mode localization as a measure of how much of the intensity of a given mode comes from a given subsystem (in this case – a waveguide). It is calculated as

$$L(k, f_n) = \frac{\mathcal{I}_\mathrm{w}}{\mathcal{I}_\mathrm{w} + \mathcal{I}_\mathrm{d}}, \tag{6}$$

where $\mathcal{I}_\mathrm{w}$ and $\mathcal{I}_\mathrm{d}$ are the intensity of the mode in the waveguide and dot, respectively. Intensity is measured as

$$\mathcal{I}_{\mathrm{w(d)}}(k, f_n) = \iiint_{V_{\mathrm{w(d)}}} |\mathbf{m}(k, f_n)|^2 \,\mathrm{d}x\,\mathrm{d}y\,\mathrm{d}z \tag{7}$$

where $V_{\mathrm{w(d)}}$ is the volume of the waveguide (dot) in a unit cell. The mode fully localized in the dot has a value of $L = 0$ and is marked in Figs. 4(b,c) with light blue color, while the mode fully localized in the waveguide has a value of $L = 1$ and is marked with light brown color.

The mode localization for the W/SD system is shown in Fig. 4(b). The SW profiles of 5 selected modes (W/SD-1–W/SD-5) are presented in the first row of Fig. 4(e). Additionally, we plot the frequency as a function of localization in Fig. 4(a). In the range I, the lowest mode has a frequency above 3 GHz, and all modes up to 8.9 GHz are predominantly confined to the waveguide with minimal amplitude in the dot. The lowest localization value in this region is $L = 0.89$. This result is consistent with the simulations of eigenstates of an isolated dot, where the lowest mode was observed at 9 GHz (see Section S1 in the Supplementary Materials). Therefore, any excitation in the dot below this frequency is only a forced oscillation. Most of the modes in this area resemble typical waveguide modes, e.g. mode W/SD-3. However, other modes, such as W/SD-1 and W/SD-2, are significantly distorted. Despite the Bragg gap being present only at the edge of the Brillouin zone, their branches are coupled throughout the entire range of the zone. This results in a non-uniform SW amplitude, even at zero k.

Above 8.9 GHz, the dispersion relation is densely populated with modes of mixed localization. In this frequency range, marked as range II, the modes have a mixed character, with a localization value in the range between 0.14 and 0.96, with the upper limit decreasing to 0.83 above 10.5 GHz. Among them, there are modes localized predominantly in the dot (e.g. mode W/SD-4), which originate from the resonant modes in the dot. However, there is always significant energy leakage to the waveguide. On the other hand, the propagating waveguide modes, such as mode W/SD-5, also have significant amplitude in the dot. The presence of the dot also strongly modifies the

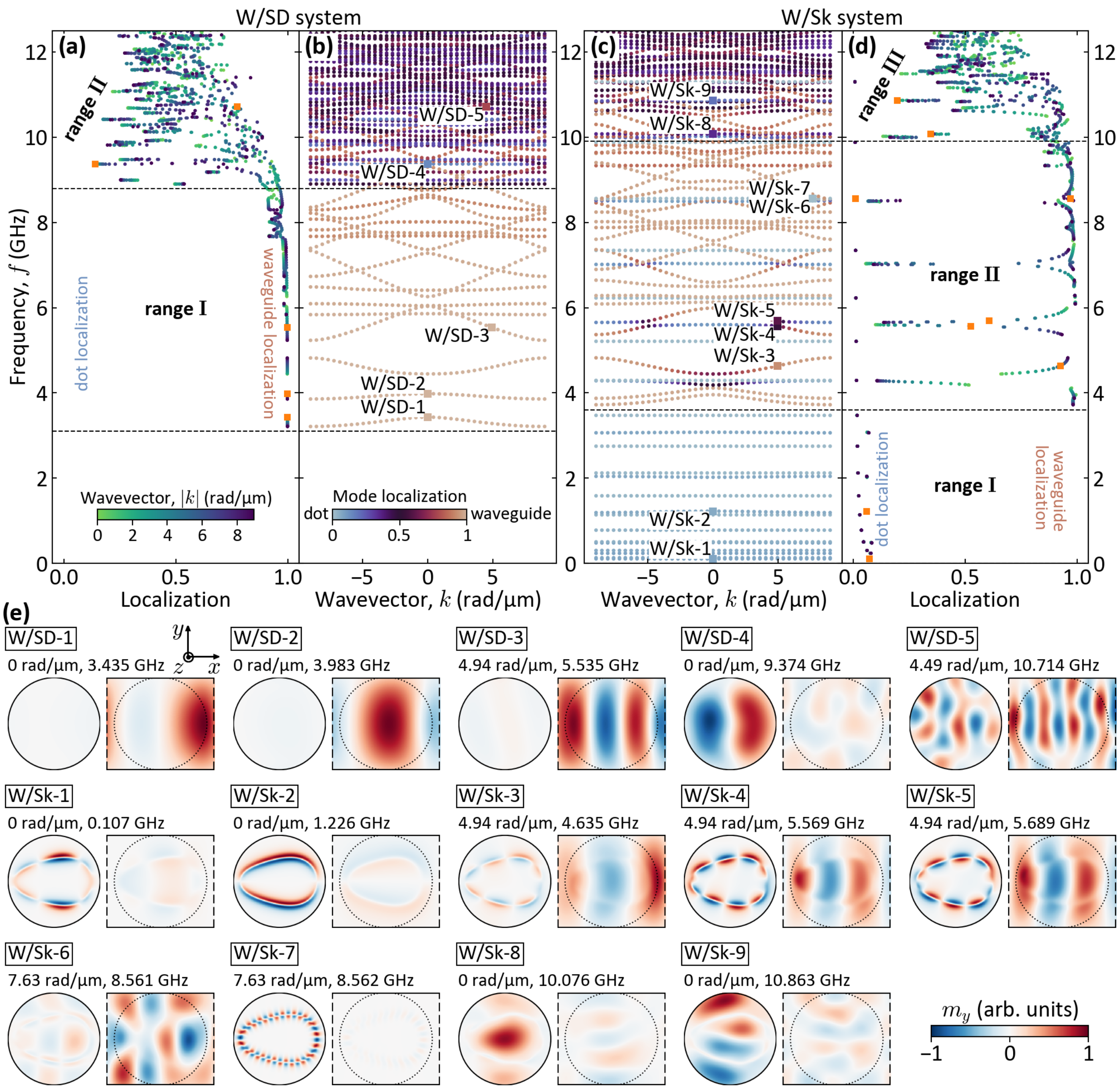

Figure 4. The dispersion relation in the first Brillouin zone presents the localization of modes in both (b) W/SD and (c) W/Sk systems. Each mode localization value is indicated by the color of the point on the dispersion. The corresponding plots with the localization value are shown in (a) for the W/SD system and in (d) for the W/Sk system. Here, the color of the point marks the absolute value of the wavevector. Dashed black vertical lines mark the limits of ranges. (e) SW mode profiles for 5 modes in the W/SD system and 9 modes in the W/Sk system. The modes are marked on the dispersion relations with a square point and a label. In each mode profile, the left color map displays the m_y magnetization component in the xy-plane at the center of the dot, while the right color map displays m_y in the xy-plane at the center of the waveguide. The intensity is normalized so that the maximum value of $|m_y|$ is 1 for each of the mode profiles. All profiles are labeled and their wavevector and frequency are given. The animated version of this figure is available in [52].

wavefront of the SW propagating in the waveguide (see mode W/SD-5). This effect can be used to excite propagating SWs in the waveguide by exciting the dots themselves, similar to the excitation of short-wavelength SWs with 2D diffraction couplers [53].

The W/Sk system exhibits different behavior, as presented in Fig. 4(c). The SW profiles of 9 selected modes are presented in two bottom rows of Fig. 4(e). Additionally, we plot the frequency as a function of localization in Fig. 4(d).

Range I spans the frequencies from 100 MHz to 3.5 GHz, which is below the frequency of the lowest waveguide band. It contains 15 flat bands related to the modes localized in dots, which are clockwise and counterclockwise azimuthal modes of the skyrmion domain wall, similar to the skyrmion in an isolated dot (see Fig. S1 in Supplementary Materials) [33]. The lowest frequency mode, W/Sk-1, is a 3rd order counterclockwise mode. The skyrmion breathing mode, W/Sk-2, has a frequency of 1.226 GHz and is only the ninth lowest mode. The largest localization in this range is $L = 0.08$. The modes in this range have very small bandwidths ranging from 9 kHz to 34 MHz (breathing mode, W/Sk-2). This is because these modes can only interact through dipolar interactions or evanescent SWs, which are the only ones that can exist in the waveguide at such low frequencies. The simulation of the dot chain in the skyrmion state but without the waveguide (see Table 1 in Section S2 of the Supplementary Materials) shows that the bandwidths of most of the bands are significantly smaller in the absence of the waveguide, except for the breathing mode (of comparable bandwidth, 33 MHz) and the fourth counterclockwise mode, which is larger than in the system with the waveguide (further details on this comparison can be found in Section S2 of the Supplementary Materials). This suggests the coupling of the skyrmion modes from the range I through the evanescent waves in the waveguide. Such an effect is similar to the enhanced SW transmission in bi-component 1D MC at frequencies below the FMR frequency of one of the constituent materials [54]. However, here it is theoretically predicted for 1D HMC consisting of a homogeneous film and a chain of dots in the skyrmion state, the system easily extendable to a 2D array. The effects described above could be exploited for the design of frequency-selective magnonic devices, enabling precise control over signal modulation and processing at the nanoscale. The distinct localization and narrow bandwidths of these modes offer opportunities to create highly-efficient filters or oscillators that operate within a precisely-defined frequency range. Furthermore, these weakly dispersive bands can be used to exploit the flat-band physics recently demonstrated in 1D MCs with periodic modulation of a DMI [39, 55].

Starting from 3.5 GHz, similarly to W/SD system, modes localized in the waveguide start to appear but they coexist with skyrmion modes in this range (marked as range II). Interestingly, the skyrmion is always slightly excited even if the mode is strongly localized in the waveguide (see mode W/Sk-3 with localization 0.925). On the one hand, the clockwise skyrmion modes hybridize with the waveguide modes, resulting in mixed modes that are confined to both the waveguide and the dot. In Fig. 4(d), these modes form characteristic horizontally-aligned points with localization between 0.05 and about 0.55. As it was shown before, such a hybridization leads to the presence of an additional band gap marked as gap 3a in Fig. 3(d), whose modes are labeled W/Sk-4 and W/Sk-5. Thus, it is possible to excite propagating modes in the waveguide with a specific wavelength by excitation of specific skyrmion modes, and study the recently intensively explored physics of the dynamically coupled systems, in particular magnon–magnon coupling [56–58]. Moreover, the resonant coupling offers a possibility for the realization of artificial neural networks [41, 42], where the propagating SWs act as synapses connecting neurons, playing through the nanodot in skyrmion or single-domain state. However, this requires the activation of neurons by propagating SWs. Such a nonlinear property can be achieved by slightly increasing the SW amplitude so that the static magnetic component decreases, resulting in a change of the resonance frequency (e.g. around the modes W/Sk-4 and W/Sk-5 or around 4 GHz, with a change of just about 10 MHz) [59–61] and, depending on the realization, activating or deactivating of the resonance effect.

On the other hand, counterclockwise skyrmion modes form a vertical line of points in Fig. 4(d) and have a strong localization in dots with L not exceeding 0.02. The interaction between counterclockwise modes and waveguide modes is negligible. Modes W/Sk-6 and W/Sk-7 differ in frequency only by 1 MHz but their localization values are 0.97 and 0.01, respectively. Moreover, the small amplitude in the dot for mode W/Sk-6 is not connected with the skyrmion mode W/Sk-7, confirming a lack of coupling between them. It points to the possibility of exploiting these modes, which are strongly localized in the dot or waveguide but are uncoupled, as bound states in the continuum. This effect that has been extensively studied in photonics but has yet to be explored in magnonics [38].

The last range, marked as range III, starts at 10 GHz, from where the dispersion is densely populated with modes having mixed localization. These modes include bulk dot modes, where the skyrmion core and the magnetization outside are excited (modes W/Sk-8 and W/Sk-9) and are coupled with the waveguide. However, counterclockwise skyrmion modes with very low localization and bandwidth below 10 kHz still exist in this range. Excluding them, the localization ranges from 0.13 to 0.96. Above 11.5 GHz, it ranges from 0.23 to 0.82. Range III starts at a higher frequency than the analogical range II in the W/SD system. This is due to the presence of skyrmion in the dot, which induces specific confinement of the resonant modes in the dot, leading to an increase in their frequency.

IV. CONCLUSIONS

We have studied a one-dimensional HMC consisting of an infinitely-long Py waveguide and a chain of nanodots with PMA and DMI (Ir/Co/Pt), in which we consider two different magnetic states: a skyrmion and a single-domain state. The static magnetization configuration in the HMC differs from that of its isolated subsystems. The configuration of the dot imprints the magnetization texture upon the waveguide, at the same time, the skyrmion shape becomes strongly distorted, taking on an egg-like shape. This makes a SW dynamic in an HMC complex while increasing the skyrmion stability and offering multifunctional properties for advancing magnonics.

The dispersion relations of both systems exhibit characteristic features of magnonic crystals, such as folded branches and band gaps. However, there is a substantial difference in the sizes of the band gaps. Additionally, the W/Sk system has a large number of flat low-frequency skyrmion modes. These modes are azimuthal rotating modes, both clockwise and counterclockwise, localized in the skyrmion domain wall and are characterized by very narrow bandwidths ranging from single kHz to single MHz. Interestingly, the bandwidths are significantly larger compared to those of the dot chain without waveguide, indicating evanescent-wave coupling between the skyrmions in W/Sk system. The flat bands may also overlap with the waveguide modes at higher frequencies and, interestingly, depending on their sense of rotation, can hybridize with them, sometimes even leading to additional band gaps in the spectrum, or be uncoupled. In the same frequency range in the W/SD system, all modes are almost exclusively localized in the waveguide.

At frequencies above 9 GHz, the resonant modes of the dots begin to appear and strongly hybridize with the waveguide modes, causing the localization of the modes to become mixed. However, in the W/Sk system, some of the modes (localized in the skyrmion domain wall) still can not interact with the waveguide at high frequencies, which promises the realization of the bound state in the continuum in magnonics.

The above-mentioned properties offer several useful functionalities for magnonics, including reconfigurability, filtering, magnon–magnon hybridizations, uncoupled SW modes in the band structure, as well as SW-skyrmion bands together with their evanescence coupling. These functionalities are suitable for the realization of magnonic artificial neural networks.

DATA AVAILIBILITY

The raw data files that support this study are available via the Zenodo repository [52].

ACKNOWLEDGMENTS

K.S. and M.K. acknowledge the financial support from National Science Centre, Poland, grants no. UMO-2020/39/I/ST3/02413 and UMO-2021/41/N/ST3/04478. K.S. acknowledges the financial support from the Foundation for Polish Science.

[1] A. V. Chumak, P. Kabos, M. Wu, C. Abert, C. Adelmann, A. O. Adeyeye, J. Akerman, F. G. Aliev, A. Anane, A. Awad, C. H. Back, A. Barman, G. E. W. Bauer, M. Becherer, E. N. Beginin, V. A. S. V. Bittencourt, Y. M. Blanter, P. Bortolotti, I. Boventer, D. A. Bozhko, S. A. Bunyaev, J. J. Carmiggelt, R. R. Cheenikundil, F. Ciubotaru, S. Cotofana, G. Csaba, O. V. Dobrovolskiy, C. Dubs, M. Elyasi, K. G. Fripp, H. Fulara, I. A. Golovchanskiy, C. Gonzalez-Ballestero, P. Graczyk, D. Grundler, P. Gruszecki, G. Gubbiotti, K. Guslienko, A. Haldar, S. Hamdioui, R. Hertel, B. Hillebrands, T. Hioki, A. Houshang, C.-M. Hu, H. Huebl, M. Huth, E. Iacocca, M. B. Jungfleisch, G. N. Kakazei, A. Khitun, R. Khymyn, T. Kikkawa, M. Klaui, O. Klein, J. W. Klos, S. Knauer, S. Koraltan, M. Kostylev, M. Krawczyk, I. N. Krivorotov, V. V. Kruglyak, D. Lachance-Quirion, S. Ladak, R. Lebrun, Y. Li, M. Lindner, R. Macedo, S. Mayr, G. A. Melkov, S. Mieszczak, Y. Nakamura, H. T. Nembach, A. A. Nikitin, S. A. Nikitov, V. Novosad, J. A. Otalora, Y. Otani, A. Papp, B. Pigeau, P. Pirro, W. Porod, F. Porrati, H. Qin, B. Rana, T. Reimann, F. Riente, O. Romero-Isart, A. Ross, A. V. Sadovnikov, A. R. Safin, E. Saitoh, G. Schmidt, H. Schultheiss, K. Schultheiss, A. A. Serga, S. Sharma, J. M. Shaw, D. Suess, O. Surzhenko, K. Szulc, T. Taniguchi, M. Urbanek, K. Usami, A. B. Ustinov, T. van der Sar, S. van Dijken, V. I. Vasyuchka, R. Verba, S. V. Kusminskiy, Q. Wang, M. Weides, M. Weiler, S. Wintz, S. P. Wolski, and X. Zhang, Advances in Magnetics Roadmap on Spin-Wave Computing, IEEE Trans. Magn. **58**, 1 (2022).

[2] Q. Wang, G. Csaba, R. Verba, A. V. Chumak, and P. Pirro, Perspective on nanoscaled magnonic networks (2023), arXiv:2311.06129 [physics.app-ph].

[3] A. V. Chumak, A. A. Serga, and B. Hillebrands, Magnon transistor for all-magnon data processing, Nat. Commun. **5**, 4700 (2014).

[4] S. Klingler, P. Pirro, T. Brächer, B. Leven, B. Hillebrands, and A. V. Chumak, Design of a spin-wave majority gate employing mode selection, Appl. Phys. Lett. **105**, 152410 (2014).

[5] T. Fischer, M. Kewenig, D. A. Bozhko, A. A. Serga, I. I. Syvorotka, F. Ciubotaru, C. Adelmann, B. Hillebrands, and A. V. Chumak, Experimental prototype of a spin-wave majority gate, Appl. Phys. Lett. **110**, 152401 (2017).

[6] M.-K. Lee and M. Mochizuki, Reservoir computing with spin waves in a skyrmion crystal, Phys. Rev. Appl. **18**, 014074 (2022).

[7] O. Lee, T. Wei, K. D. Stenning, J. C. Gartside, D. Prestwood, S. Seki, A. Aqeel, K. Karube, N. Kanazawa, Y. Taguchi, C. Back, Y. Tokura, W. R. Branford, and H. Kurebayashi, Task-adaptive physical reservoir computing, Nat. Mater. **23**, 79 (2024).

[8] S. Wintz, V. Tiberkevich, M. Weigand, J. Raabe, J. Lindner, A. Erbe, A. Slavin, and J. Fassbender, Magnetic vortex cores as tunable spin-wave emitters, Nat. Nanotechnol. **11**, 948 (2016).

[9] H. Yu, J. Xiao, and H. Schultheiss, Magnetic texture based magnonics, Phys. Rep. **905**, 1 (2021).

[10] D. Petti, S. Tacchi, and E. Albisetti, Review on magnonics with engineered spin textures, J. Phys. D: Appl. Phys.

55, 293003 (2022).

[11] A. Fert, V. Cros, and J. Sampaio, Skyrmions on the track, Nat. Nanotechnol. **8**, 152 (2013).

[12] M. Lonsky and A. Hoffmann, Dynamic excitations of chiral magnetic textures, APL Mater. **8**, 100903 (2020).

[13] K.-W. Moon, B. S. Chun, W. Kim, and C. Hwang, Control of spin-wave refraction using arrays of skyrmions, Phys. Rev. Appl. **6**, 064027 (2016).

[14] J. Lan and J. Xiao, Skew scattering and side jump of spin wave across magnetic texture, Phys. Rev. B **103**, 054428 (2021).

[15] Z. Wang, H. Y. Yuan, Y. Cao, Z.-X. Li, R. A. Duine, and P. Yan, Magnonic frequency comb through nonlinear magnon-skyrmion scattering, Phys. Rev. Lett. **127**, 037202 (2021).

[16] S. A. Díaz, T. Hirosawa, D. Loss, and C. Psaroudaki, Spin wave radiation by a topological charge dipole, Nano Lett. **20**, 6556 (2020).

[17] H. Vakili, J.-W. Xu, W. Zhou, M. N. Sakib, M. G. Morshed, T. Hartnett, Y. Quessab, K. Litzius, C. T. Ma, S. Ganguly, M. R. Stan, P. V. Balachandran, G. S. D. Beach, S. J. Poon, A. D. Kent, and A. W. Ghosh, Skyrmionics—Computing and memory technologies based on topological excitations in magnets, J. Appl. Phys. **130**, 070908 (2021).

[18] K. Everschor-Sitte, J. Masell, R. M. Reeve, and M. Kläui, Perspective: Magnetic skyrmions—Overview of recent progress in an active research field, J. Appl. Phys. **124**, 240901 (2018).

[19] A. Fert, N. Reyren, and V. Cros, Magnetic skyrmions: advances in physics and potential applications, Nat. Rev. Mater. **2**, 17031 (2017).

[20] C. H. Marrows and K. Zeissler, Perspective on skyrmion spintronics, Appl. Phys. Lett. **119**, 250502 (2021).

[21] D. Prychynenko, M. Sitte, K. Litzius, B. Krüger, G. Bourianoff, M. Kläui, J. Sinova, and K. Everschor-Sitte, Magnetic skyrmion as a nonlinear resistive element: A potential building block for reservoir computing, Phys. Rev. Appl. **9**, 014034 (2018).

[22] K. M. Song, J.-S. Jeong, B. Pan, X. Zhang, J. Xia, S. Cha, T.-E. Park, K. Kim, S. Finizio, J. Raabe, J. Chang, Y. Zhou, W. Zhao, W. Kang, H. Ju, and S. Woo, Skyrmion-based artificial synapses for neuromorphic computing, Nat. Electron. **3**, 148 (2020).

[23] M. S. N. Tey, X. Chen, A. Soumyanarayanan, and P. Ho, Chiral spin textures for next-generation memory and unconventional computing, ACS Appl. Electron. Mater. **4**, 5088 (2022).

[24] A. Dhiman, M. Matczak, R. Gieniusz, I. Sveklo, Z. Kurant, U. Guzowska, F. Stobiecki, and A. Maziewski, Thickness dependence of interfacial Dzyaloshinskii-Moriya interaction, magnetic anisotropy and spin waves damping in Pt/Co/Ir and Ir/Co/Pt trilayers, J. Magn. Magn. Mater. **519**, 167485 (2021).

[25] S. Azzawi, A. T. Hindmarch, and D. Atkinson, Magnetic damping phenomena in ferromagnetic thin-films and multilayers, J. Phys. D: Appl. Phys. **50**, 473001 (2017).

[26] N. Tang, W. L. N. C. Liyanage, S. A. Montoya, S. Patel, L. J. Quigley, A. J. Grutter, M. R. Fitzsimmons, S. Sinha, J. A. Borchers, E. E. Fullerton, L. DeBeer-Schmitt, and D. A. Gilbert, Skyrmion-excited spin-wave fractal networks, Adv. Mater. **35**, 2300416 (2023).

[27] C. Jin, S. Li, H. Zhang, R. Wang, J. Wang, R. Lian, P. Gong, and X. Shi, Spin-wave modes of elliptical skyrmions in magnetic nanodots, New J. Phys. **24**, 043005 (2022).

[28] M. Zelent, P. Gruszecki, M. Moalic, O. Hellwig, A. Barman, and M. Krawczyk, Chapter One - Spin dynamics in patterned magnetic multilayers with perpendicular magnetic anisotropy (Academic Press, 2022) pp. 1–51.

[29] K. Y. Guslienko and Z. V. Gareeva, Gyrotropic skyrmion modes in ultrathin magnetic circular dots, IEEE Magn. Lett. **8**, 1 (2017).

[30] J.-V. Kim, F. Garcia-Sanchez, J. Sampaio, C. Moreau-Luchaire, V. Cros, and A. Fert, Breathing modes of confined skyrmions in ultrathin magnetic dots, Phys. Rev. B **90**, 064410 (2014).

[31] M. Mruczkiewicz, P. Gruszecki, M. Zelent, and M. Krawczyk, Collective dynamical skyrmion excitations in a magnonic crystal, Phys. Rev. B **93**, 174429 (2016).

[32] M. Garst, J. Waizner, and D. Grundler, Collective spin excitations of helices and magnetic skyrmions: review and perspectives of magnonics in non-centrosymmetric magnets, J. Phys. D: Appl. Phys. **50**, 293002 (2017).

[33] M. Mruczkiewicz, P. Gruszecki, M. Krawczyk, and K. Y. Guslienko, Azimuthal spin-wave excitations in magnetic nanodots over the soliton background: Vortex, Bloch, and Néel-like skyrmions, Phys. Rev. B **97**, 064418 (2018).

[34] Z. Chen and F. Ma, Skyrmion based magnonic crystals, J. Appl. Phys. **130**, 090901 (2021).

[35] I. A. Golovchanskiy, N. N. Abramov, V. S. Stolyarov, P. S. Dzhumaev, O. V. Emelyanova, A. A. Golubov, V. V. Ryazanov, and A. V. Ustinov, Ferromagnet/superconductor hybrid magnonic metamaterials, Adv. Sci. **6**, 1900435 (2019).

[36] J. Chen, J. Hu, and H. Yu, Chiral emission of exchange spin waves by magnetic skyrmions, ACS Nano **15**, 4372 (2021).

[37] M. Zelent, M. Moalic, M. Mruczkiewicz, X. Li, Y. Zhou, and M. Krawczyk, Stabilization and racetrack application of asymmetric Néel skyrmions in hybrid nanostructures, Sci. Rep. **13**, 13572 (2023).

[38] C. W. Hsu, B. Zhen, A. D. Stone, J. D. Joannopoulos, and M. Soljacic, Bound states in the continuum, Nat. Rev. Mater. **1**, 16048 (2016).

[39] R. A. Gallardo, D. Cortés-Ortuño, T. Schneider, A. Roldán-Molina, F. Ma, R. E. Troncoso, K. Lenz, H. Fangohr, J. Lindner, and P. Landeros, Flat bands, indirect gaps, and unconventional spin-wave behavior induced by a periodic Dzyaloshinskii-Moriya interaction, Phys. Rev. Lett. **122**, 067204 (2019).

[40] D. D. Awschalom, C. R. Du, R. He, F. J. Heremans, A. Hoffmann, J. Hou, H. Kurebayashi, Y. Li, L. Liu, V. Novosad, J. Sklenar, S. E. Sullivan, D. Sun, H. Tang, V. Tyberkevych, C. Trevillian, A. W. Tsen, L. R. Weiss, W. Zhang, X. Zhang, L. Zhao, and C. W. Zollitsch, Quantum engineering with hybrid magnonic systems and materials, IEEE Trans. Quantum Eng. **2**, 1 (2021).

[41] Á. Papp, W. Porod, and G. Csaba, Nanoscale neural network using non-linear spin-wave interference, Nat. Commun. **12**, 6422 (2021).

[42] K. G. Fripp, Y. Au, A. V. Shytov, and V. V. Kruglyak, Nonlinear chiral magnonic resonators: Toward magnonic neurons, Appl. Phys. Lett. **122**, 172403 (2023).

[43] K. Szulc, S. Tacchi, A. Hierro-Rodríguez, J. Díaz, P. Gruszecki, P. Graczyk, C. Quirós, D. Markó,

J. I. Martín, M. Vélez, D. S. Schmool, G. Carlotti, M. Krawczyk, and L. M. Álvarez Prado, Reconfigurable magnonic crystals based on imprinted magnetization textures in hard and soft dipolar-coupled bilayers, ACS Nano **16**, 14168 (2022).

[44] K. Guslienko and Z. Gareeva, Magnetic skyrmion low frequency dynamics in thin circular dots, J. Magn. Magn. Mater. **442**, 176 (2017).

[45] M. Zelent, J. Tóbik, M. Krawczyk, K. Y. Guslienko, and M. Mruczkiewicz, Bi-stability of magnetic skyrmions in ultrathin multilayer nanodots induced by magnetostatic interaction, Phys. Status Solidi RRL **11**, 1700259 (2017).

[46] I. Lemesh and G. S. D. Beach, Twisted domain walls and skyrmions in perpendicularly magnetized multilayers, Phys. Rev. B **98**, 104402 (2018).

[47] S. Woo, K. Litzius, B. Krüger, M.-Y. Im, L. Caretta, K. Richter, M. Mann, A. Krone, R. M. Reeve, M. Weigand, P. Agrawal, I. Lemesh, M.-A. Mawass, P. Fischer, M. Kläui, and G. S. D. Beach, Observation of room-temperature magnetic skyrmions and their current-driven dynamics in ultrathin metallic ferromagnets, Nat. Mater. **15**, 501 (2016).

[48] A. Suna, Perpendicular magnetic ground state of a multilayer film, J. Appl. Phys. **59**, 313 (1986).

[49] I. V. Vetrova, M. Zelent, J. Šoltýs, V. A. Gubanov, A. V. Sadovnikov, T. Šcepka, J. Dérer, R. Stoklas, V. Cambel, and M. Mruczkiewicz, Investigation of self-nucleated skyrmion states in the ferromagnetic/nonmagnetic multilayer dot, Appl. Phys. Lett. **118**, 212409 (2021).

[50] A. Riveros, F. Tejo, J. Escrig, K. Guslienko, and O. Chubykalo-Fesenko, Field-dependent energy barriers of magnetic Néel skyrmions in ultrathin circular nanodots, Phys. Rev. Appl. **16**, 014068 (2021).

[51] G. Gubbiotti, L. L. Xiong, F. Montoncello, L. Giovannini, and A. O. Adeyeye, Spin wave dispersion and intensity correlation in width-modulated nanowire arrays: A Brillouin light scattering study, J. Appl. Phys. **124**, 083903 (2018).

[52] K. Szulc, Dataset for "Reconfigurable spin-wave platform based on interplay between nanodots and waveguide in hybrid magnonic crystal" (2024), https://doi.org/10.5281/zenodo.10964849.

[53] H. Yu, O. d'Allivy Kelly, V. Cros, R. Bernard, P. Bortolotti, A. Anane, F. Brandl, F. Heimbach, and D. Grundler, Approaching soft X-ray wavelengths in nanomagnet-based microwave technology, Nat. Commun. **7**, 11255 (2016).

[54] H. Qin, G.-J. Both, S. J. Hämäläinen, L. Yao, and S. van Dijken, Low-loss YIG-based magnonic crystals with large tunable bandgaps, Nat. Commun. **9**, 5445 (2018).

[55] S. Tacchi, J. Flores-Farías, D. Petti, F. Brevis, A. Cattoni, G. Scaramuzzi, D. Girardi, D. Cortés-Ortuno, R. A. Gallardo, E. Albisetti, G. Carlotti, and P. Landeros, Experimental observation of flat bands in one-dimensional chiral magnonic crystals, Nano Lett. **23**, 6776 (2023).

[56] K. Adhikari, S. Choudhury, S. Barman, Y. Otani, and A. Barman, Observation of magnon-magnon coupling with high cooperativity in $Ni_{80}Fe_{20}$ cross-shaped nanoring array, Nanotechnology **32**, 395706 (2021).

[57] J. C. Gartside, A. Vanstone, T. Dion, K. D. Stenning, D. M. Arroo, H. Kurebayashi, and W. R. Branford, Reconfigurable magnonic mode-hybridisation and spectral control in a bicomponent artificial spin ice, Nat. Commun. **12**, 2488 (2021).

[58] Y. Wang, Y. Zhang, C. Li, J. Wei, B. He, H. Xu, J. Xia, X. Luo, J. Li, J. Dong, W. He, Z. Yan, W. Yang, F. Ma, G. Chai, P. Yan, C. Wan, X. Han, and G. Yu, Ultrastrong to nearly deep-strong magnon-magnon coupling with a high degree of freedom in synthetic antiferromagnets, Nat. Commun. **15**, 2077 (2024).

[59] P. Krivosik and C. E. Patton, Hamiltonian formulation of nonlinear spin-wave dynamics: Theory and applications, Phys. Rev. B **82**, 184428 (2010).

[60] H. Merbouche, B. Divinskiy, K. O. Nikolaev, C. Kaspar, W. H. P. Pernice, D. Gouerne, R. Lebrun, V. Cros, J. Ben Youssef, P. Bortolotti, A. Anane, S. O. Demokritov, and V. E. Demidov, Giant nonlinear self-phase modulation of large-amplitude spin waves in microscopic YIG waveguides, Sci. Rep. **12**, 7246 (2022).

[61] Q. Wang, R. Verba, B. Heinz, M. Schneider, O. Wojewoda, K. Davidkova, K. Levchenko, C. Dubs, N. J. Mauser, M. Urbánek, P. Pirro, and A. V. Chumak, Deeply nonlinear excitation of self-normalized short spin waves, Sci. Adv. **9**, eadg4609 (2023).

Supplementary Materials
Reconfigurable spin-wave platform based on interplay between nanodots and waveguide in hybrid magnonic crystal

Krzysztof Szulc,* Mateusz Zelent, and Maciej Krawczyk
Institute of Spintronics and Quantum Information, Faculty of Physics, Adam Mickiewicz University, Poznań, Uniwersytetu Poznańskiego 2, 61-614 Poznań, Poland

We present a hybrid magnonic crystal composed of a chain of nanodots with strong perpendicular magnetic anisotropy and Dzyaloshinskii–Moriya interaction, positioned above a permalloy waveguide. The study examines two different magnetization states in the nanodots: a single-domain state and an egg-shaped skyrmion state. Due to the dipolar coupling between the dot and the waveguide, a strongly bound hybrid magnetization texture is formed in the system. Our numerical results show complex spin-wave spectra, combining the effects of periodicity, magnetization texture, and hybridization of the propagating waves in the waveguide with the dot/skyrmion modes. The systems are characterized by different band gap sizes. For the skyrmion state, the azimuthal modes confined to the skyrmion domain wall lead to the formation of flat bands at low frequencies, while at higher frequencies we identify among them modes interacting with the propagating waves, which can introduce additional non-Bragg band gaps, as well as isolated modes leading to the formation of bound states. On the other hand, the system with a single-domain state in nanodots offers a wide range of frequencies where the spin waves are predominantly in the waveguide. Thus, the study shows that the proposed hybrid magnonic crystals have many distinct functionalities, highlighting their reconfigurable potential, magnon–magnon couplings, mode localization, and bound states overlapping with the propagating waves. This opens up potential applications in analog and quantum magnonics, spin-wave filtering, and the establishment of magnonic neural networks.

S1. THE DYNAMICS OF ISOLATED SUBSYSTEMS

Figure S1(a) shows the comparison between the dynamics of the isolated subsystems. The dispersion relation of an isolated waveguide is shown with solid blue lines. The resonant modes of a dot are shown with horizontal dashed lines: orange line for an isolated dot in the single-domain state and green line for an isolated dot in the skyrmion state.

The lowest zero-k frequency of the waveguide is 4.04 GHz and it reaches a minimum of 3.76 GHz for $k = 9.0\,\mathrm{rad/\mu m}$. Higher-order modes have their minima at 6.19 GHz, 8.17 GHz, 9.92 GHz, and 11.57 GHz, respectively. First four modes exhibit a backward-wave regime at small wavevectors, while higher modes can only propagate forward.

In case of the dot, its static configuration has a very large impact on the frequency of resonant modes. In a single-domain state, the lowest mode has a frequency of 8.89 GHz and it is a fundamental mode (SD-1). Modes with higher frequencies are clockwise (CW) [e.g. SD-2] and counterclockwise (CCW) [e.g. SD-3] azimuthal modes, as well as higher-order radial modes (e.g. SD-4).

The skyrmion state exhibits numerous low-frequency modes, which are all CW (e.g. Sk-1) and CCW (e.g. Sk-3) azimuthal modes in the skyrmion domain wall, except of one skyrmion breathing mode (Sk-2) (which can be considered the 0th order azimuthal mode). The first mode not associated with the skyrmion domain wall is the fundamental mode of a skyrmion core (Sk-4) at the frequency 9.47 GHz. The higher-frequency modes includes higher-order azimuthal and radial modes, which can be localized either in the skyrmion core (e.g. Sk-5), outside the skyrmion (e.g. Sk-7) or in both the core and outside (e.g. Sk-6). Interestingly, some of the skyrmion domain wall modes in this range can also be strongly excited outside the skyrmion (e.g. Sk-8).

S2. COMPARISON BETWEEN W/SK SYSTEM AND A DOT CHAIN

In order to investigate the contribution of the dipolar interaction between the dot and the waveguide to the bandwidth of the skyrmion domain wall modes, we studied a one-dimensional chain of dots in skyrmion state, which is a subsystem of the W/Sk system. Additionally, as a reference, we studied a single dot in a skyrmion state.

Table I shows the simulation data for the modes within the frequency range I of the W/Sk system, as depicted in Fig. 4(c,d) in the main manuscript. This range contains 15 modes, ranging from the 2nd CW to the 12th CCW mode. Modes at higher frequencies may be significantly impacted by interaction with waveguide modes and are therefore not included in Table I.

First of all, it is important to note that the static configurations of these systems are different. In a single dot, the skyrmion is round. In a dot chain, the dipolar interaction between the dots is very small so the skyrmion re-

* krzysztof.szulc@amu.edu.pl

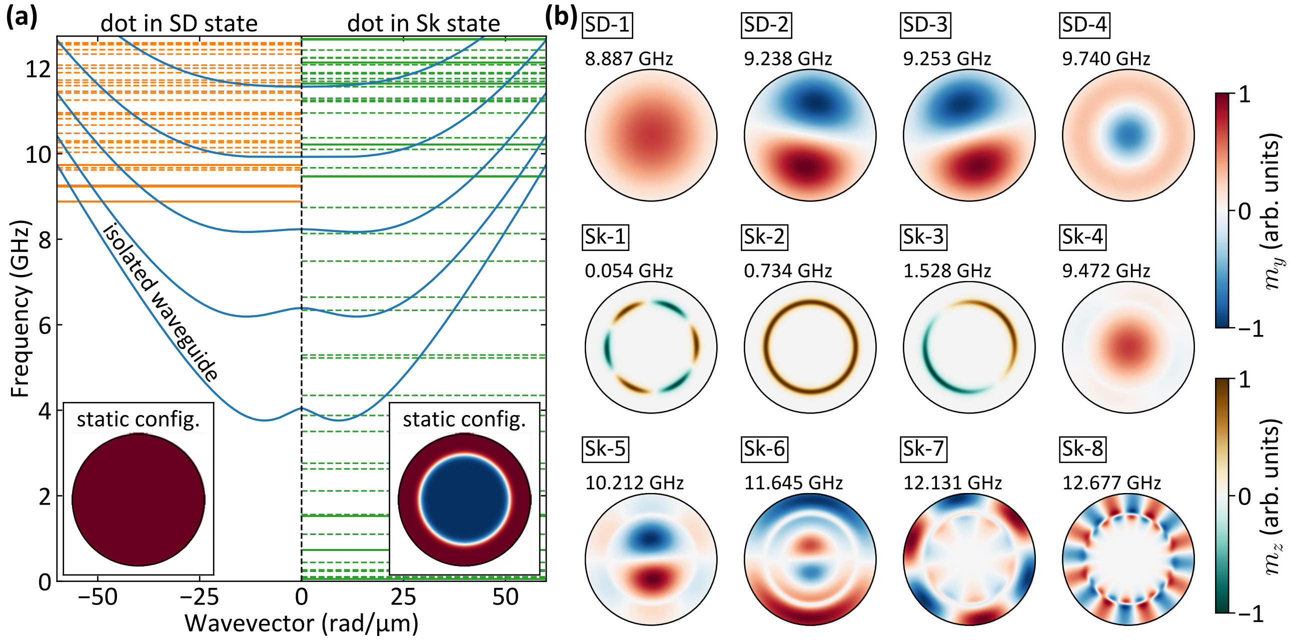

Figure S1. (a) Dispersion relation of an isolated waveguide (solid blue lines) and frequencies of the resonant modes of a dot in a single-domain state (horizontal dashed orange lines) and in a skyrmion state (horizontal dashed green lines). Solid orange and green lines correspond to the modes which profiles are shown in (b). Please note that the resonant modes are characterized solely by their frequencies and they are not connected with the wavevector presented on the horizontal axis. The division of the single-domain state and skyrmion modes on the negative and positive wavevector sides is made solely for the sake of presentation clarity. (b) Resonant mode profiles of the dot of four modes in the SD state and eight modes in the Sk state. Please note that all SD modes and Sk-4 – Sk-8 modes are presented with m_y component (top color bar), while modes Sk-1 – Sk-3 are presented with m_z component (bottom color bar). All modes are normalized to the maximum absolute value of the mode. The animated version of this figure is available in [52].

mains round. In the W/Sk system, the skyrmion changes its shape to an egg-like shape, as shown in Fig. 2(c) in the main manuscript. This change in shape significantly impacts the mode frequencies. As shown in Table I, the frequencies of modes in a single dot and an array of dots are very similar, differing by no more than 65 MHz. On the other hand, modes in the W/Sk system can differ from a single dot modes as much as 516 MHz for the 1st CW mode. However, for the higher-order CCW modes, this difference is strongly reduced.

When comparing the bandwidths of the same modes in different systems, it is clear that the dipolar interaction between the dot and the waveguide significantly contributes to this value. The bandwidths of all modes, except of the 4th CCW mode, are larger in W/Sk system, indicating that the presence of the waveguide enhance the interaction between the skyrmions. This effect is particularly noticeable for higher-order CCW modes (5th order and higher), whose bandwidths are orders of magnitude larger in the W/Sk system. However, it is difficult to distinguish the contribution of modified static configuration of a skyrmion and dynamic dipolar interaction through the waveguide.

Table I. The comparison of the skyrmion domain wall modes in three different systems: single dot, dot chain, and W/Sk system as defined in the main manuscript. For a single dot, we present the value of the mode frequency, while for dot chain and W/Sk system, we show the lowest and the highest frequency of the band and the bandwidth. Please note that the frequencies are in MHz, while bandwidths are in kHz.

	Single dot	Dot chain			W/Sk system		
Mode	f (MHz)	$f_{\min}$ (MHz)	$f_{\max}$ (MHz)	Bandwidth (kHz)	$f_{\min}$ (MHz)	$f_{\max}$ (MHz)	Bandwidth (kHz)
CW 2	2628	2627	2628	1309.06	3065	3078	13085.05
CW 1	1528	1542	1549	7533.08	2023	2044	21187.33
breathing	734	747	780	33223.62	1192	1226	34143.46
CCW 1	266	290	296	5996.20	482	490	8453.12
CCW 2	91	106	107	354.05	238	239	1061.96
CCW 3	54	64	64	42.51	107	108	533.27
CCW 4	106	117	117	264.79	132	133	178.41
CCW 5	235	237	237	13.78	303	304	728.22
CCW 6	441	438	438	2.25	505	505	208.15
CCW 7	729	719	719	1.99	780	781	265.48
CCW 8	1101	1083	1083	0.96	1140	1140	26.74
CCW 9	1561	1534	1534	8.47	1586	1586	36.19
CCW 10	2113	2075	2075	0.10	2122	2122	9.06
CCW 11	2760	2710	2710	0.08	2750	2750	11.54
CCW 12	3504	3440	3440	0.01	3474	3474	54.62